On the Role of Long-Range Electrostatics in Machine-Learned Interatomic Potentials for Complex Battery Materials

Carsten G. Staacke, Hendrik H. Heenen, Christoph Scheurer, Gábor Csányi, Karsten Reuter, and Johannes T. Margraf*

Read Online

ACCESS | Metrics & More | Article Recommendations | Supporting Information

ABSTRACT: Modeling complex energy materials such as solid-state electrolytes (SSEs) realistically at the atomistic level strains the capabilities of state-of-the-art theoretical approaches. On one hand, the system sizes and simulation time scales required are prohibitive for first-principles methods such as the density functional theory. On the other hand, parameterizations for empirical potentials are often not available, and these potentials may ultimately lack the desired predictive accuracy. Fortunately, modern machine learning (ML) potentials are increasingly able to bridge this gap, promising first-principles accuracy at a much reduced computational cost. However, the local nature of these ML potentials typically means that long-range contributions arising, for example, from electrostatic interactions are neglected. Clearly, such interactions can be large in polar materials such as electrolytes, however. Herein, we investigate the effect that the locality assumption of ML potentials has on lithium mobility and defect formation energies in the SSE $Li_7P_3S_{11}$. We find that neglecting long-range electrostatics is unproblematic for the description of lithium transport in the isotropic bulk. In contrast, (field-dependent) defect formation energies are only adequately captured by a hybrid potential combining ML and a physical model of electrostatic interactions. Broader implications for ML-based modeling of energy materials are discussed.

KEYWORDS: machine learning, electrostatics, battery, solid-state electrolyte, locality
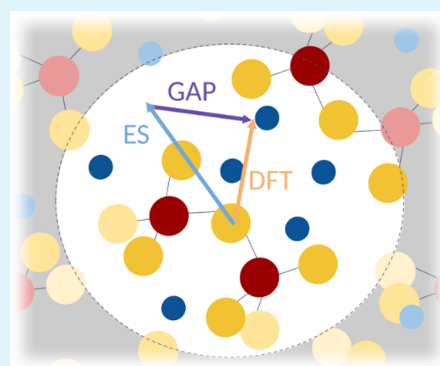
1. INTRODUCTION

The development of new analytical approximation frameworks is currently leading to an unparalleled surge of machine learning (ML) approaches in all areas of chemistry and materials science.[1–5] Here, ML is typically considered a universal approach for learning (fitting) a complex relationship $y = f(x)$ without explicitly knowing the physical (analytic) form of f.[6,7] In the context of interatomic potentials, this means establishing the relationship between a system's atomistic structure and its total energy $E = f(\{Z, R\})$, where Z are the atomic numbers and R are the position vectors of the constituting atoms. The expectation here is that flexible ML potentials can overcome long-standing limitations of empirical potentials that use simple fixed functional forms.[7]

Such limitations are especially acute when covalent bonds are formed or broken, when atoms vary their hybridization or charge state, and generally when large changes in chemical environments occur. All these aspects apply prominently to the simulation of *operando* energy conversion systems in general and battery materials in particular.[3,8–15] With the structural and compositional complexity of contemporary battery materials severely limiting direct first-principles-based simulations, there is thus considerable hope that ML potentials trained with first-principles data will enable simulations at

unprecedented length and time scales and a predictive quality matching that of electronic structure methods.[16–23]

To achieve size extensivity and create a general ML potential that can be employed for systems of varying size and composition, just as with many empirical potentials (*e.g.*, embedded atom models and Tersoff potentials), a locality assumption is typically made.[6,7,24] The system's total energy is thus approximated as a sum of local (atomic) contributions

$$E = \sum_{i}^{N} \epsilon(Z_i, \chi_i) \tag{1}$$

where the sum runs over the N atoms in the system and each atom i contributes with an energy ϵ that only depends on its atomic number Z_i and its local chemical environment χ_i (which is itself a function of $\{Z, R\}$). This local environment is suitably encoded into a representation that (similar to the total energy)
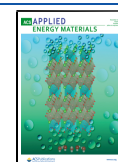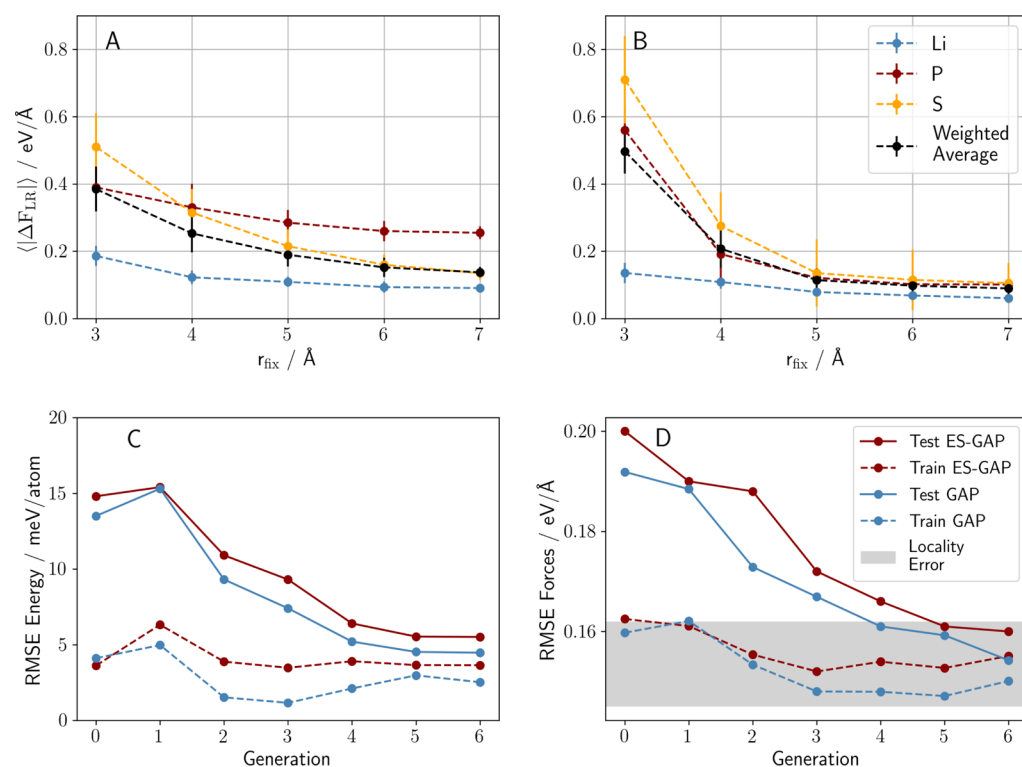
Figure 1. (A) Force locality in crystalline $Li_7P_3S_{11}$. (B) Force locality in crystalline $Li_7P_3S_{11}$ after subtracting the ES baseline model. Convergence of energies (C) and forces (D) throughout the generations for both models (GAP: blue and ES-GAP: red). Solid lines correspond to test errors and dashed lines to training errors. The gray shading corresponds to the expected force accuracy according to the locality test.

obeys general symmetries such as the invariance to translation, rotation, and permutation of atoms of the same element.[6,7,25−27] Importantly, to allow for efficient training and scalability to large simulation cells, these representations are almost always short-ranged, that is, they only describe the environment within a few Ångstroms around each atom.

In recent years, a large variety of ML potentials using kernel- or neural-network-based regression has been developed for molecular and condensed systems, heralding the great potential of this new data-driven approach.[6,7,28] Notably, such short-ranged ML potentials have also been applied to polar systems such as water.[29−32] Though one would naively expect long-range electrostatic interactions to play a significant role here, these potentials provide a remarkably accurate description of the structural and dynamic properties of bulk liquid water and different ice phases.[33] This is presumably because these systems are highly isotropic so that long-range interactions average out.[34] Consequently, short-ranged ML potentials are now commonly applied to study polar and even ionic systems.[30,35−37]

However, the importance of long-range effects will clearly depend on the material and property of interest and thus demands more systematic scrutiny.[38] For example, ionic diffusion in electrolytes may lead to the transient local accumulation and depletion of charges, which can break the isotropy of the electrostatic environment. Even more critically, grain-boundaries, interfaces, and defects may lead to a permanent localized polarization of materials. Finally, the effect of applied electric fields, for example, in batteries, can obviously only be studied if an electrostatic description is part of the model.

Notably, several groups have recently proposed ML models that explicitly include long-range electrostatics.[39−45] These range from simple point-charge models to polarizable models and full self-consistent approximations of the charge density. While these approaches offer a route to overcome the locality constraints of current ML potentials, they also lead to an increased computational cost, both in terms of training and evaluation. In particular, they break the favorable linear scaling of the computational cost with the system size. This makes it crucial to understand when such explicit treatments of electrostatics are necessary and when a local ML potential can be used instead.

The goal of this paper is to analyze the effect of electrostatic contributions on ML-based simulations of battery materials, using the Li mobility and interface stability of the crystalline phase of the solid-state electrolyte (SSE) $Li_7P_3S_{11}$ as an example.[46,47] $Li_7P_3S_{11}$ exhibits an exceptionally high Li-ion conductivity and has been suggested as a promising candidate for all-solid-state lithium batteries.[46,47] Large-scale simulations of this material, possible, for example, through Gaussian approximation potentials (GAPs), can provide critical insights into solving open challenges in connection with this material.

We develop two GAP models where one is strictly short-ranged (GAP), while the other includes a simple electrostatic baseline (ES-GAP). We find that the inclusion of long-range ES interactions only benefits the description of nonisotropic chemical environments, while diffusion properties in the homogeneous bulk material are well-captured by both potentials. In contrast, the stability of Frenkel defects in the presence of electric fields (which influence the material's stability at the inhomogeneous electrode/electrolyte interface) can only be captured with a model that includes long-range interactions.

2. METHODS

2.1. Computational Details. Reference density functional theory (DFT) calculations are performed with the Perdew–Burke–Ernzerhof functional, default "light" integration grids, and a "tier 1" basis set of numerical atomic orbitals, as implemented in FHI-aims.[48,49] The Brillouin zone is sampled with a $2 \times 2 \times 2$ k-grid. Initial training configurations are generated with *ab initio* molecular dynamics (AIMD) using the Γ-point approximation for the k-grid. GAP-based MD and nudged-elastic-band (NEB) simulations are performed using the LAMMPS[50] code and the corresponding interface to QUIP.[51] Pairwise electrostatic interactions in the ES-GAP model are included *via* a fixed-charge model. To avoid the divergence of point-charge Coulomb interaction at short distances, atomic charge densities are modeled by s-type Slater orbitals as, for example, in the QEq charge equilibration model.[52,53] Further details on the ES-GAP are noted in Section A of the Supporting Information. For training set construction and data analysis, the atomic simulation environment, SciPy, and scikit-learn are used.[54−56]

2.2. GAP Training. To train the GAP models, a simple iterative procedure is used. Briefly, an initial model is trained on a set of 80 crystalline $Li_7P_3S_{11}$ configurations, taken from a short DFT-based MD simulation and Monte Carlo-sampled Li-ion distributions on crystal and interstitial sites. This potential is then used to generate new configurations *via* MD simulations at 800 K, which are added to the training set. This procedure is repeated for several iterations (termed "generations") until the force and energy errors on new configurations no longer improve. The thus-obtained models provide an increasingly accurate description of high-temperature crystalline $Li_7P_3S_{11}$. GAP and ES-GAP models are trained on identical configurations, and the ES-GAP model was used to generate new configurations in the iterative procedure. Further details can be found in the Supporting Information Section C.

3. RESULTS

3.1. GAP and ES-GAP Models. As discussed above, a hallmark of many-body ML potentials is the assumption that the total energy can be described as a sum of local atomic contributions, which corresponds to a complete neglect of long-range interactions. The locality of these interactions is thus often tacitly assumed when ML potentials are generated. However, it can also be quantified more rigorously by analyzing the force ΔF_{LR} induced on a reference atom by perturbations of other atoms in the distance beyond a given cutoff radius.[57] This locality test is performed with the reference method before fitting an ML potential and can thus be considered the material property. Figure 1A shows the mean induced force and its standard deviation for $Li_7P_3S_{11}$ (see the Supporting Information for details).

As can be seen, the induced forces are quite large (between 0.1 and 0.5 eV/Å) and decay slowly with the cutoff. This is particularly evident for the phosphorous atoms, which bear the largest formal charge in this system (+5). Importantly, these forces are by construction long-ranged since they exclusively originate from perturbations beyond the given radius. They therefore cannot be described by an ML potential with the corresponding cutoff. In this sense, the mean induced force $\langle |\Delta F_{LR}| \rangle$ provides a lower bound for the residual force errors that an ML potential with a given cutoff can achieve.

In Figure 1B, the same locality test is performed after subtracting the fixed-charge ES baseline model from the DFT forces (see the Supporting Information for details). For cutoffs larger than 5 Å, this significantly lowers $\langle |\Delta F_{LR}| \rangle$, most prominently for phosphorous. Counterintuitively, the induced forces on phosphorous and sulfur are actually increased at shorter distances. On one hand, this is because the charges of

this model were parameterized to minimize the locality error at 6 Å and are thus not ideal for shorter cutoffs. On the other hand, a fixed-charge ES model is generally inaccurate for short-range interactions, where polarization, charge transfer, and induction effects become important. To capture such effects with a baseline model would require the use of more complex polarizable models. Nonetheless, cutoffs of 6 Å are commonly used in state-of-the-art ML potentials so that a fixed charge ES baseline can be used here, though residual errors remain and are discussed below.

The convergence of the iterative training procedure can be seen in Figure 1C,D. This shows that the energy and force errors of both models show no further improvement between the fifth and sixth generations. Importantly, the final force errors fall into the expected range estimated from the locality test (see Figure 1B). This indicates the convergence of the training process, meaning that the remaining error will not be significantly reduced by further training but is instead related to the locality of the model and/or potential inadequacies of the representation.

Interestingly, the root mean squared errors (RMSEs) for predicted energies and forces are actually slightly lower for the short-range GAP model. By analyzing the errors of the individual elements separately (see the Supporting Information), we find that the ES-GAP displays somewhat higher errors for sulfur but lower errors for lithium and especially phosphorous. Since sulfur is the most abundant element in $Li_7P_3S_{11}$, this leads to the better average performance of the short-range GAP.

This points to a disadvantage of the fixed-charge approach used here: $Li_7P_3S_{11}$ features two distinct sulfur species, namely, in bridging and terminal positions. Hirshfeld population analysis (see the Supporting Information) indicates that these species correspond to different charge states, while they are treated equivalently by the ES baseline. This introduces an error, which needs to be compensated by the GAP potential. In principle, this could be mitigated by assigning different charges to these sulfur species. However, such atom typing would run counter to one of the main advantages of ML potentials relative to classical force-fields, namely, the fact that they can break and form bonds. A more satisfying solution would be the use of floating-charge models, and this will be explored in future work.[42,58]

From a different perspective, the differences in force errors observed for different elements also illustrate a weakness in average error metrics such as the RMSE (or the least-squares loss function minimized by the GAP) for multispecies systems: if the stoichiometry of a material is not balanced, more abundant species are implicitly weighted more strongly by the metric. In the present case, sulfur has the largest weight, although lithium is arguably more important. Nevertheless, the accuracy of both models is actually quite satisfying overall, considering the magnitudes of the force components in the training and test sets, which range up to ca. 10 eV/Å. Note, however, that in principle, it would be possible to use different weightings in the loss function for forces on different elements. In GAP models, this can be achieved by specifying individual regularization parameters for each force.[59]

3.2. Lithium-Ion Mobility. Both potentials introduced in the previous section are trained on the same data and have approximately the same force error, though small differences can be seen when looking at the description of individual elements. Do these differences affect the prediction of the
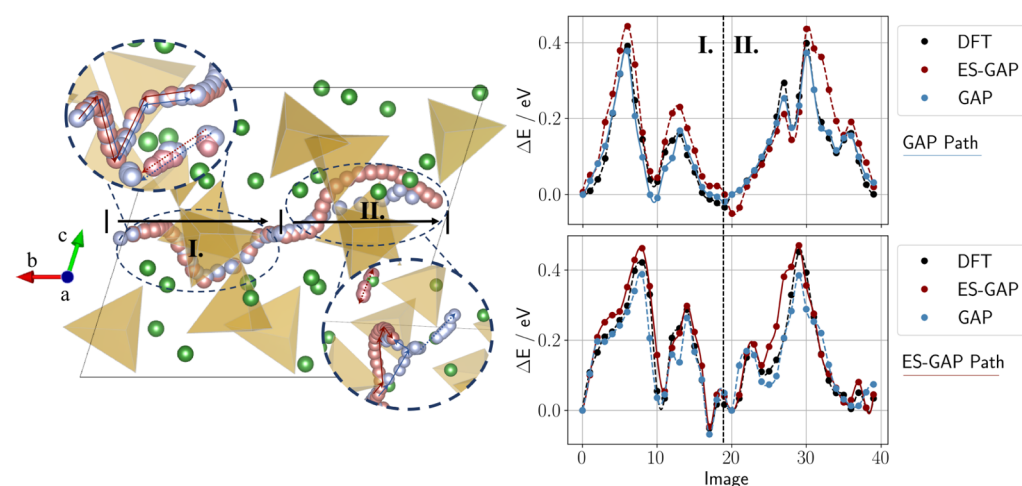
Figure 2. Left: Illustration of minimum-energy paths for lithium diffusion through $Li_7P_3S_{11}$ obtained with short-range GAP (light blue) and ES-GAP (red) interatomic potentials. Li ions are shown as green spheres and thiophosphates as orange tetrahedra. Solid and dashed arrows highlight the main migration path and displacements of neighboring lithium atoms, respectively. The labels I and II indicate two consecutive NEB calculations. Initial and final positions are obtained by analyzing hopping events from MD trajectories (see Supporting Information Section G). Right: Energies for DFT, GAP, and ES-GAP potentials on the minimum-energy paths calculated with the short-range GAP (top) and the ES-GAP (bottom). Solid lines indicate the potential with which the path was obtained and dashed lines indicate single-point calculations.

observables relevant to battery performance? As the first case in point, we investigate the Li-ion mobility in the (isotropic) bulk material. To this end, we consider lithium diffusion barriers obtained *via* the NEB method (see Figure 2) and Li-ion mobilities obtained from MD simulations.

NEB calculations allow the investigation of minimum-energy paths of individual Li hops between two equilibrium positions (an initial state and a final state).[60] Choosing these states is actually nontrivial since $Li_7P_3S_{11}$ contains a large variety of possible Li interstitial positions, reflecting the highly dynamic nature of the Li sublattice. This was previously demonstrated by Chang *et al.*, who reported a number of Li configurations with nearly the same ground-state energy as that of the equilibrium crystal structure.[61,62] It is therefore important to focus on Li hopping events that actually contribute to conductivity and not just dynamic rearrangements of Li positions.

To obtain these relevant pathways, we therefore analyzed the training MD trajectories to isolate individual Li hopping events. In this manner, a variety of diffusion pathways were obtained. Further information on all pathways is given in the Supporting Information (Section G). In the following, the lowest-barrier pathway is discussed in more detail. Here, a Li ion diffuses in a channel formed by the PS_4^- and $P_2S_7^-$ anion complexes (positions are tabulated in the Supporting Information Section G), along the *b* lattice vector, as shown in Figure 2. It can be seen that the $1 \times 2 \times 1$ supercell is traversed with two consecutive Li-ion hops (obtained from two NEB calculations Figure 2 I,II). These NEB calculations were performed based on both the GAP and ES-GAP potentials, leading to slightly different minimum-energy paths.

Nevertheless, the optimized lowest-energy paths display similar characteristics of a correlated ion migration where lithium ions diffuse, while neighboring ions are slightly displaced from the diffusion path (highlighted in the figure with solid and dashed arrows for the migrating and displaced atoms, respectively). For the first hop, an almost identical path is found, while the second hop yields a slightly different path when optimized with the two potentials (I and II in Figure 2,

respectively). The deviating paths should not be understood as different mechanisms favored by the respective potentials, however, but merely as two feasible paths found by the NEB. We confirm this assumption by evaluating the energies along the short-range GAP path with the ES-GAP (and vice-versa). This analysis reveals almost identical barrier heights for a given potential on both its own NEB path and the one from the other potential. It is further noteworthy that the ES-GAP consistently predicts somewhat higher barriers than the short-range GAP. For both paths, reference DFT single-point values tend to lie between the GAP and ES-GAP values. In other words, the GAP somewhat underestimates the barriers, while the ES-GAP overestimates them to a similar degree. The deviation in energies is also not perfectly uniform along the paths so that the agreement with the DFT can be excellent for both potentials, at different points of the potential energy surface.

Despite the overall similar performance of the models, we thus find small systematic differences between the predictions of the two models. Interestingly, the short-range GAP is actually slightly more accurate in predicting the lowest barrier heights. This indicates that the static-charge model used for the ES-GAP does not faithfully reflect the electrostatics of the full DFT calculation, and the ES baseline represents an over-correction: it correctly increases the barriers but by too much. As a sidenote, we emphasize that both models are mainly trained on high-temperature MD data, while the NEB corresponds to the minimum energy path at 0 K. Presumably, an even higher accuracy for NEB calculations could be achieved for both potentials by training on the corresponding data.

Next, we turn to the Li-ion conductivity σ at finite temperature, predicted from MD simulations *via* the Nernst−Einstein equation (see the Supporting Information for details). Here, we shift the focus from a microscopic property (the Li migration barrier height) to a macroscopic observable (Li-ion conductivity). In principle, the two are closely related since the barrier height determines the rate of the Li transport in the transition state theory. However, MD

simulations sample a multitude of different diffusion events. These are often dominated by the lowest barrier mechanism but may also be influenced by higher barrier pathways (*e.g.*, because they are entropically favored). In this sense, the NEB and MD simulations provide complementary information.

The corresponding conductivities within the two potentials (at 800 K) are shown in Figure 3 as a function of the MD
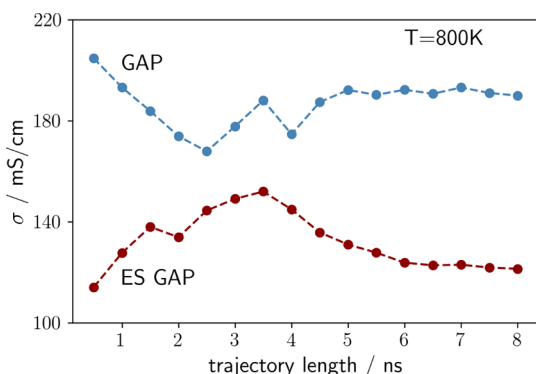
Figure 3. Convergence of the Li-ion conductivity σ at 800 K during an MD simulation. The red curve corresponds to the ES-GAP model and blue to the GAP model.

trajectory length. After sufficient sampling, the conductivities converge to 190 mS/cm for the GAP and 120 mS/cm for the ES-GAP. This trend in conductivities perfectly reflects the NEB barrier differences discussed above (*i.e.*, slightly higher mobility and lower barriers for the short-range GAP model).

Figure 3 also highlights the benefit of using ML potentials for battery research more generally: to obtain fully converged conductivities from these simulations, MD trajectory lengths far beyond the tractability of typical AIMD simulations are necessary. Hence, AIMD simulations of Li-ion conductivities should generally not be considered converged and yield, at best, a qualitative indicator of relative performance between closely related materials. Even at longer timescales in the low-nanosecond range (<5 ns), conductivity differences predicted by both models vary from 10 to 80%.

While we do find some differences between the predicted Li mobilities of the ES-GAP and GAP, these should be put into perspective. Ion mobilities of potential SSE materials can vary by several orders of magnitude, and the small differences in observed barrier heights are certainly within the margin of the DFT error. From a practical perspective, there is thus no significant difference between the two models.[63] At this point, one could conclude from a practitioner's point of view that a short-ranged ML potential would be fully sufficient to treat a complex battery material such as $Li_7P_3S_{11}$.

More broadly speaking, the observed insensitivity of energetic and dynamic properties of bulk $Li_7P_3S_{11}$ to long-range electrostatics is also in line with the previous reports on other polar liquids and solids.[29−32] For dynamic properties, electrostatic screening by mobile ions is clearly a significant cause of this behavior. Nonetheless, it is notable that the ES-GAP and GAP also perform very similarly in static calculations, as illustrated by the energy−volume curve of $Li_7P_3S_{11}$ (see the Supporting Information). This is a consequence of the fact that the crystalline system studied herein is highly isotropic. As a consequence, long-range interactions contribute to a large but nearly constant Madelung potential. These contributions

cancel each other out to a large extent when considering forces and relative energies.

3.3. Applied Fields and Defects. Having established the similar behavior of the GAP and ES-GAP for bulk Li mobilities, we now turn to their description of an anisotropic environment. Specifically, we consider a model system that mimics the effect of the potential drop in the interphase region at the solid/solid interface between an electrode and an SSE. This potential variation has been previously computed using a 1-D continuum model[64] for a Li anode and graphite (C) cathode setup (see Figure 4). In this model, the potential drop
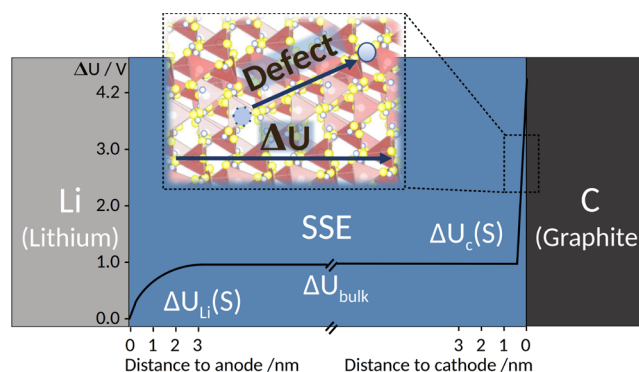

Figure 4. Schematic of the spatially dependent potential variation ΔU in a prototypical Li‖SSE‖C solid-state Li-ion battery.[64] Since the grain orientation varies throughout the SSE, the field-dependent defect stability is studied by applying electric fields along different crystallographic axes of the simulation cell.

reaches several nanometers into the bulk region before it is completely screened by displaced ions. To model the effect of this potential drop on the SSE near the interface, we apply electric fields to a $2 \times 3 \times 2$ $Li_7P_3S_{11}$ supercell and investigate how the field strength and direction affect the stability of a Frenkel defect (*i.e.*, a Li vacancy/interstitial pair).

Defects have been argued to play an important role in the kinetics of the decomposition processes at SSE interfaces.[65] This kinetic stability is of high relevance to the applicability of SSEs.[66−68] Here, we consider a Frenkel defect in particular as it allows keeping the simulation cell overall charge neutral and lies within the phase space covered by the training set of the GAP potentials. Clearly, the effect of an electric potential drop can only be captured by the ES-GAP model, which contains charges that are able to respond to the applied field. In contrast, the short-range GAP model can only model the "zero-field" scenario. We also compare the "zero-field" defect stability in both models with that in the DFT.

We construct the Frenkel defect by shifting a Li atom into an interstitial position and relaxing the resulting structure using the two GAP models (see Figure 5 and Supporting Information Section I). For comparison, single-point DFT calculations are also performed on both the GAP and ES-GAP geometries. Without an applied field, this leads to a predicted defect formation energy of ca. 0.8 eV with the ES-GAP and DFT and ca. 0.6 eV with the short-range GAP model. Since the interstitial Li ion has a net positive charge and the ion vacancy a net negative charge, the defect forms a dipole. The observed 0.2 eV deviation of the defect formation energies between the GAP and DFT can thus be attributed to the absence of long-range dipole−dipole interactions in the former. Notably, the formation energies of neutral Li vacancies, where such dipoles
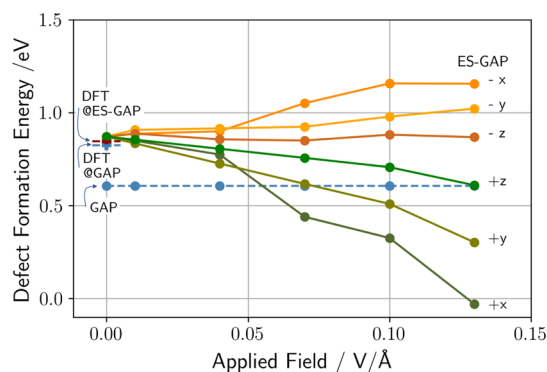
Figure 5. Frenkel defect formation energies against the applied field. The electric field is applied along the different crystallographic axes (x, y, z). Solid lines (green and orange) correspond to ES-GAP calculations with different applied field directions. Defect positions are given in the Supporting Information I.

are absent, reportedly do not show such a strong dependence on long-range electrostatics.[16]

Nonetheless, all models predict defect formation to be highly unfavorable. When applying an electric field, this picture changes. We find an anisotropic response to the field where both the destabilization and stabilization can occur (Figure 5). This anisotropy reflects the fields' orientation relative to the defect dipole. Structural relaxation effects then lead to an unsymmetric stabilization/destabilization of the defect in either field direction.

While this is a rather simple model system, it already yields insights into the stability of $Li_7P_3S_{11}$ at the SSE/electrode interface. As shown in Figure 5, field strengths typically occurring at this interface (which can reach up to 0.3 V/Å[64]) are sufficient to make the formation of this defect energetically favorable. Consequently, one would expect an accumulation of such defects toward the interface. As recently suggested,[66] the kinetic processes in electrolyte decomposition can be related to the delithiation of the SSE. Intermediate to this delithiation process are local concentration gradients by Frenkel defects. We can therefore hypothesize from our findings that local fields play a crucial role in the evaluation of interphase stabilities. Further, we find that the defect stabilization is anisotropic to the crystallographic orientation. This finding might explain the previous observations that the SSE/anode interface stability of $Li_7P_3S_{11}$ was dependent on the crystallographic orientation of the latter.[69]

From a methodological perspective, this example shows that the explicit inclusion of electrostatic interactions will be indispensable for the computational study of battery materials under operating conditions. Indeed, even the contact between two different materials will cause a potential drop across the interface, albeit at a smaller length scale.[13] The good performance of the short-range GAP model in the previous section is thus not because long-range electrostatic interactions are small but because they are reasonably isotropic in a periodic calculation. Breaking this symmetry with an interface or by applying an electric field clearly shows the importance of electrostatics which, by design, cannot be incorporated into a model with a short-range cutoff.

We note that the response of the ES-GAP model to the applied field relies on the ionic partial charges of the baseline ES model. Hence, we exploited the corresponding *a priori* knowledge. Ideally, these charges could instead be determined

in the training procedure, including model structures of the full interface, which, however, is beyond the scope of this conceptual study.

4. CONCLUSIONS

In this paper, we have systematically explored the influence of explicitly including electrostatic interactions in ML potentials for battery materials. Using the same ML approach and training data, we find significant differences between a short-range GAP model and the ES-GAP model that uses an ES baseline when studying isotropic *versus* nonisotropic systems. In standard isotropic simulation tasks, such as determining Li diffusion barriers and ionic conductivities, both models yield similar results. In contrast, simulations on nonisotropic systems show the importance of ES contributions and provide new insights into the interphase stability of $Li_7P_3S_{11}$.

Specifically, we studied Frenkel defects in an applied field, mimicking the potential drop at a solid/solid interface. In this setup, we found that the stabilization of the defects can occur already at moderate fields. This would favor the accumulation of defects toward the interphase, which could influence the kinetic stability of $Li_7P_3S_{11}$/electrode interfaces. Additionally, such stabilizations are anisotropic to the crystallographic orientation, making the grain shape and orientation an additional parameter to be considered in battery engineering and beyond.[70]

More generally, our results confirm that short-ranged ML potentials can be surprisingly accurate for polar and ionic materials in the absence of nonisotropic chemical environments such as interfaces or electric fields. In contrast, we found important qualitative deviation between our GAP models in nonisotropic systems. The further development of ML potentials with an explicit description of electrostatics therefore represents an important research goal on the way to the computational study of battery materials in *operando* conditions.

■ ASSOCIATED CONTENT

Ⓢ Supporting Information

The Supporting Information is available free of charge at https://pubs.acs.org/doi/10.1021/acsaem.1c02363.

> GAP model details, locality test and locality-based charge fit, interstitial configurations via Voronoi tessellation, ionic mobility, species-resolved model convergence, charge analysis, NEB calculations and interstitial Li position, defect positions, and energy–volume curve (PDF)

■ AUTHOR INFORMATION

Corresponding Author

Johannes T. Margraf − *Chair for Theoretical Chemistry and Catalysis Research Center, Technische Universität München, D-85747 Garching, Germany; Fritz-Haber-Institut der Max-Planck-Gesellschaft, D-14195 Berlin, Germany;* orcid.org/0000-0002-0862-5289; Email: margraf@fhi.mpg.de

Authors

Carsten G. Staacke − *Chair for Theoretical Chemistry and Catalysis Research Center, Technische Universität München, D-85747 Garching, Germany; Fritz-Haber-Institut der Max-Planck-Gesellschaft, D-14195 Berlin, Germany*

Hendrik H. Heenen − *Fritz-Haber-Institut der Max-Planck-Gesellschaft, D-14195 Berlin, Germany;* ⬤ orcid.org/0000-0003-0696-8445

Christoph Scheurer − *Chair for Theoretical Chemistry and Catalysis Research Center, Technische Universität München, D-85747 Garching, Germany; Fritz-Haber-Institut der Max-Planck-Gesellschaft, D-14195 Berlin, Germany*

Gábor Csányi − *Engineering Laboratory, University of Cambridge, Cambridge CB2 1PZ, U.K.*

Karsten Reuter − *Chair for Theoretical Chemistry and Catalysis Research Center, Technische Universität München, D-85747 Garching, Germany; Fritz-Haber-Institut der Max-Planck-Gesellschaft, D-14195 Berlin, Germany*

Complete contact information is available at:
https://pubs.acs.org/10.1021/acsaem.1c02363

◼ REFERENCES

(1) von Lilienfeld, O. A.; Müller, K.-R.; Tkatchenko, A. Exploring chemical compound space with quantum-based machine learning. *Nat. Rev. Chem.* **2020**, *4*, 347−358.

(2) Cheng, B.; Griffiths, R.-R.; Wengert, S.; Kunkel, C.; Stenczel, T.; Zhu, B.; Deringer, V. L.; Bernstein, N.; Margraf, J. T.; Reuter, K.; Csanyi, G. Mapping Materials and Molecules. *Acc. Chem. Res.* **2020**, *53*, 1981−1991.

(3) Deringer, V. L. Modelling and Understanding Battery Materials with Machine-Learning-Driven Atomistic Simulations. *J. Phys. Energy* **2020**, *2*, 041003.

(4) Stocker, S.; Csányi, G.; Reuter, K.; Margraf, J. T. Machine Learning in Chemical Reaction Space. *Nat. Commun.* **2020**, *11*, 5505.

(5) Noé, F.; Tkatchenko, A.; Müller, K.-R.; Clementi, C. Machine Learning for Molecular Simulation. *Annu. Rev. Phys. Chem.* **2020**, *71*, 361.

(6) Bartók, A. P.; Payne, M. C.; Kondor, R.; Csányi, G. Gaussian approximation potentials: The accuracy of quantum mechanics, without the electrons. *Phys. Rev. Lett.* **2010**, *104*, 136403.

(7) Behler, J.; Parrinello, M. Generalized neural-network representation of high-dimensional potential-energy surfaces. *Phys. Rev. Lett.* **2007**, *98*, 146401.

(8) Artrith, N.; Urban, A.; Ceder, G. Constructing First-Principles Phase Diagrams of Amorphous LixSi Using Machine-Learning-Assisted Sampling with an Evolutionary Algorithm. *J. Chem. Phys.* **2018**, *148*, 241711.

(9) Urban, A.; Seo, D.-H.; Ceder, G. Computational Understanding of Li-Ion Batteries. *npj Comput. Mater.* **2016**, *2*, 16002.

(10) Stegmaier, S.; Schierholz, R.; Povstugar, I.; Barthel, J.; Rittmeyer, S. P.; Yu, S.; Wengert, S.; Rostami, S.; Kungl, H.; Reuter, K.; Eichel, R. A.; Scheurer, C. Nano-Scale Complexions Facilitate Li Dendrite-Free Operation in LATP Solid-State Electrolyte. *Adv. Energy Mater.* **2021**, *11*, 2100707.

(11) Heenen, H. H.; Voss, J.; Scheurer, C.; Reuter, K.; Luntz, A. C. Multi-ion Conduction in Li3OCl Glass Electrolytes. *J. Phys. Chem. Lett.* **2019**, *10*, 2264−2269.

(12) Heenen, H. H.; Scheurer, C.; Reuter, K. Implications of occupational disorder on ion mobility in Li4Ti5O12 battery materials. *Nano Lett.* **2017**, *17*, 3884−3888.

(13) Stegmaier, S.; Voss, J.; Reuter, K.; Luntz, A. C. Li+ defects in a solid-state Li ion battery: theoretical insights with a Li3OCl electrolyte. *Chem. Mater.* **2017**, *29*, 4330−4340.

(14) Bruix, A.; Margraf, J. T.; Andersen, M.; Reuter, K. First-principles-based multiscale modelling of heterogeneous catalysis. *Nat. Catal.* **2019**, *2*, 659−670.

(15) Timmermann, J.; Kraushofer, F.; Resch, N.; Li, P.; Wang, Y.; Mao, Z.; Riva, M.; Lee, Y.; Staacke, C.; Schmid, M.; Scheurer, C.; Parkinson, G. S.; Diebold, U.; Reuter, K. IrO2 Surface Complexions Identified through Machine Learning and Surface Investigations. *Phys. Rev. Lett.* **2020**, *125*, 206101.

(16) Li, W.; Ando, Y.; Minamitani, E.; Watanabe, S. Study of Li Atom Diffusion in Amorphous Li3PO4 with Neural Network Potential. *J. Chem. Phys.* **2017**, *147*, 214106.

(17) Onat, B.; Cubuk, E. D.; Malone, B. D.; Kaxiras, E. Implanted Neural Network Potentials: Application to Li-Si Alloys. *Phys. Rev. B* **2018**, *97*, 094106.

(18) Lacivita, V.; Artrith, N.; Ceder, G. Structural and Compositional Factors That Control the Li-Ion Conductivity in LiPON Electrolytes. *Chem. Mater.* **2018**, *30*, 7077−7090.

(19) Deng, Z.; Chen, C.; Li, X.-G.; Ong, S. P. An Electrostatic Spectral Neighbor Analysis Potential for Lithium Nitride. *npj Comput. Mater.* **2019**, *5*, 75.

(20) Wang, C.; Aoyagi, K.; Wisesa, P.; Mueller, T. Lithium Ion Conduction in Cathode Coating Materials from On-the-Fly Machine Learning. *Chem. Mater.* **2020**, *32*, 3741−3752.

(21) Jalem, R.; Kanamori, K.; Takeuchi, I.; Nakayama, M.; Yamasaki, H.; Saito, T. Bayesian-Driven First-Principles Calculations for Accelerating Exploration of Fast Ion Conductors for Rechargeable Battery Application. *Sci. Rep.* **2018**, *8*, 5845.

(22) Houchins, G.; Viswanathan, V. An Accurate Machine-Learning Calculator for Optimization of Li-Ion Battery Cathodes. *J. Chem. Phys.* **2020**, *153*, 054124.

(23) Fujikake, S.; Deringer, V. L.; Lee, T. H.; Krynski, M.; Elliott, S. R.; Csányi, G. Gaussian Approximation Potential Modeling of Lithium Intercalation in Carbon Nanostructures. *J. Chem. Phys.* **2018**, *148*, 241714.

(24) Jung, H.; Stocker, S.; Kunkel, C.; Oberhofer, H.; Han, B.; Reuter, K.; Margraf, J. T. Size-Extensive Molecular Machine Learning with Global Representations. *ChemSystemsChem* **2020**, *2*, No. e1900052.

(25) Drautz, R. Atomic cluster expansion for accurate and transferable interatomic potentials. *Phys. Rev. B* **2019**, *99*, 014104.

(26) Faber, F. A.; Christensen, A. S.; Huang, B.; von Lilienfeld, O. A. Alchemical and Structural Distribution Based Representation for Universal Quantum Machine Learning. *J. Chem. Phys.* **2018**, *148*, 241717.

(27) Christensen, A. S.; Bratholm, L. A.; Faber, F. A.; Anatole von Lilienfeld, O. FCHL Revisited: Faster and More Accurate Quantum Machine Learning. *J. Chem. Phys.* **2020**, *152*, 044107.

(28) Shapeev, A. V. Moment tensor potentials: A class of systematically improvable interatomic potentials. *Multiscale Model. Simul.* **2016**, *14*, 1153−1173.

(29) Monserrat, B.; Brandenburg, J. G.; Engel, E. A.; Cheng, B. Extracting ice phases from liquid water: why a machine-learning water model generalizes so well. **2020**, arXiv preprint arXiv:2006.13316.

(30) Cooper, A. M.; Kästner, J.; Urban, A.; Artrith, N. Efficient Training of ANN Potentials by Including Atomic Forces via Taylor Expansion and Application to Water and a Transition-Metal Oxide. *npj Comput. Mater.* **2020**, *6*, 54.

(31) Schran, C.; Behler, J.; Marx, D. Automated Fitting of Neural Network Potentials at Coupled Cluster Accuracy: Protonated Water Clusters as Testing Ground. *J. Chem. Theory Comput.* **2020**, *16*, 88−99.

(32) Schran, C.; Brieuc, F.; Marx, D. Transferability of Machine Learning Potentials: Protonated Water Neural Network Potential Applied to the Protonated Water Hexamer. *J. Chem. Phys.* **2021**, *154*, 051101.

(33) Cheng, B.; Engel, E. A.; Behler, J.; Dellago, C.; Ceriotti, M. Ab initio thermodynamics of liquid and solid water. *PNAS* **2019**, *116*, 1110−1115.

(34) Cox, S. J. Dielectric response with short-ranged electrostatics. *PNAS* **2020**, *117*, 19746−19752.

(35) Vandermause, J.; Torrisi, S. B.; Batzner, S.; Xie, Y.; Sun, L.; Kolpak, A. M.; Kozinsky, B. On-the-fly active learning of interpretable Bayesian force fields for atomistic rare events. *npj Comput. Mater.* **2020**, *6*, 20.

(36) Jinnouchi, R.; Lahnsteiner, J.; Karsai, F.; Kresse, G.; Bokdam, M. Phase Transitions of Hybrid Perovskites Simulated by Machine-Learning Force Fields Trained on the Fly with Bayesian Inference. *Phys. Rev. Lett.* **2019**, *122*, 225701.

(37) Tovey, S.; Narayanan Krishnamoorthy, A.; Sivaraman, G.; Guo, J.; Benmore, C.; Heuer, A.; Holm, C. DFT Accurate Interatomic Potential for Molten NaCl from Machine Learning. *J. Phys. Chem. C* **2020**, *124*, 25760−25768.

(38) Yue, S.; Muniz, M. C.; Calegari Andrade, M. F.; Zhang, L.; Car, R.; Panagiotopoulos, A. Z. When do short-range atomistic machine-learning models fall short? *J. Chem. Phys.* **2021**, *154*, 034111.

(39) Faraji, S.; Ghasemi, S. A.; Rostami, S.; Rasoulkhani, R.; Schaefer, B.; Goedecker, S.; Amsler, M. High Accuracy and Transferability of a Neural Network Potential through Charge Equilibration for Calcium Fluoride. *Phys. Rev. B* **2017**, *95*, 104105.

(40) Ghasemi, S. A.; Hofstetter, A.; Saha, S.; Goedecker, S. Interatomic Potentials for Ionic Systems with Density Functional Accuracy Based on Charge Densities Obtained by a Neural Network. *Phys. Rev. B* **2015**, *92*, 045131.

(41) Grisafi, A.; Fabrizio, A.; Meyer, B.; Wilkins, D. M.; Corminboeuf, C.; Ceriotti, M. Transferable Machine-Learning Model of the Electron Density. *ACS Cent. Sci.* **2019**, *5*, 57−64.

(42) Ko, T. W.; Finkler, J. A.; Goedecker, S.; Behler, J. A fourth-generation high-dimensional neural network potential with accurate electrostatics including non-local charge transfer. *Nat. Commun.* **2021**, *12*, 398.

(43) Unke, O. T.; Meuwly, M. PhysNet: A Neural Network for Predicting Energies, Forces, Dipole Moments, and Partial Charges. *J. Chem. Theory Comput.* **2019**, *15*, 3678−3693.

(44) Xie, X.; Persson, K. A.; Small, D. W. Incorporating Electronic Information into Machine Learning Potential Energy Surfaces via Approaching the Ground-State Electronic Energy as a Function of Atom-Based Electronic Populations. *J. Chem. Theory Comput.* **2020**, *16*, 4256−4270.

(45) Yao, K.; Herr, J. E.; Toth, D. W.; McKintyre, R.; Parkhill, J. The TensorMol-0.1 Model Chemistry: A Neural Network Augmented with Long-Range Physics. *Chem. Sci.* **2018**, *9*, 2261−2269.

(46) Busche, M. R.; Weber, D. A.; Schneider, Y.; Dietrich, C.; Wenzel, S.; Leichtweiss, T.; Schröder, D.; Zhang, W.; Weigand, H.; Walter, D.; Sedlmaier, S. J.; Houtarde, D.; Nazar, L. F.; Janek, J. In Situ Monitoring of Fast Li-Ion Conductor Li7P3S11 Crystallization Inside a Hot-Press Setup. *Chem. Mater.* **2016**, *28*, 6152−6165.

(47) Dietrich, C.; Weber, D. A.; Sedlmaier, S. J.; Indris, S.; Culver, S. P.; Walter, D.; Janek, J.; Zeier, W. G. Lithium ion conductivity in Li2S-P2S5 glasses - building units and local structure evolution during the crystallization of superionic conductors Li3PS4, Li7P3S11 and Li4P2S7. *J. Mater. Chem. A* **2017**, *5*, 18111−18119.

(48) Perdew, J. P.; Burke, K.; Ernzerhof, M. Generalized Gradient Approximation Made Simple. *Phys. Rev. Lett.* **1996**, *77*, 3865.

(49) Blum, V.; Gehrke, R.; Hanke, F.; Havu, P.; Havu, V.; Ren, X.; Reuter, K.; Scheffler, M. Ab initio molecular simulations with numeric atom-centered orbitals. *Comput. Phys. Commun.* **2009**, *180*, 2175−2196.

(50) Plimpton, S. Fast parallel algorithms for short-range molecular dynamics. *J. Comput. Phys.* **1995**, *117*, 1−19.

(51) Bartók, A. P.; Kondor, R.; Csányi, G. On representing chemical environments. *Phys. Rev. B: Condens. Matter Mater. Phys.* **2013**, *87*, 184115.

(52) Rappe, A. K.; Goddard, W. A., III Charge equilibration for molecular dynamics simulations. *J. Phys. Chem.* **1991**, *95*, 3358−3363.

(53) Streitz, F. H.; Mintmire, J. W. Electrostatic potentials for metal-oxide surfaces and interfaces. *Phys. Rev. B: Condens. Matter Mater. Phys.* **1994**, *50*, 11996.

(54) Hjorth Larsen, A.; et al. The atomic simulation environment-a Python library for working with atoms. *J. Phys.: Condens. Matter* **2017**, *29*, 273002.

(55) Virtanen, P.; et al. SciPy 1.0: Fundamental Algorithms for Scientific Computing in Python. *Nat. Methods* **2020**, *17*, 261−272.

(56) Pedregosa, F.; et al. Scikit-learn: Machine Learning in Python. *J. Mach. Learn. Res.* **2011**, *12*, 2825−2830.

(57) Deringer, V. L.; Csányi, G. Machine learning based interatomic potential for amorphous carbon. *Phys. Rev. B* **2017**, *95*, 094203.

(58) Unke, O. T.; Meuwly, M. PhysNet: A neural network for predicting energies, forces, dipole moments, and partial charges. *J. Chem. Theory Comput.* **2019**, *15*, 3678−3693.

(59) Deringer, V. L.; Bartók, A. P.; Bernstein, N.; Wilkins, D. M.; Ceriotti, M.; Csányi, G. Gaussian Process Regression for Materials and Molecules. *Chem. Rev.* **2021**, *121*, 10073−10141.

(60) Henkelman, G.; Uberuaga, B. P.; Jónsson, H. A climbing image nudged elastic band method for finding saddle points and minimum energy paths. *J. Chem. Phys.* **2000**, *113*, 9901−9904.

(61) Chang, D.; Oh, K.; Kim, S. J.; Kang, K. Super-ionic conduction in solid-state Li7P3S11-type sulfide electrolytes. *Chem. Mater.* **2018**, *30*, 8764−8770.

(62) Yamane, H.; Shibata, M.; Shimane, Y.; Junke, T.; Seino, Y.; Adams, S.; Minami, K.; Hayashi, A.; Tatsumisago, M. Crystal structure of a superionic conductor, Li7P3S11. *Solid State Ionics* **2007**, *178*, 1163−1167.

(63) Döpking, S.; Plaisance, C. P.; Strobusch, D.; Reuter, K.; Scheurer, C.; Matera, S. Addressing global uncertainty and sensitivity in first-principles based microkinetic models by an adaptive sparse grid approach. *J. Chem. Phys.* **2018**, *148*, 034102.

(64) Luntz, A. C.; Voss, J.; Reuter, K. Interfacial challenges in solid-state Li ion batteries. *J. Phys. Chem. Lett.* **2015**, *6*, 4599−4604.

(65) Hong, L.; Yang, K.; Tang, M. A mechanism of defect-enhanced phase transformation kinetics in lithium iron phosphate olivine. *npj Comput. Mater.* **2019**, *5*, 118.

(66) Schwietert, T. K.; Arszelewska, V. A.; Wang, C.; Yu, C.; Vasileiadis, A.; de Klerk, N. J. J.; Hageman, J.; Hupfer, T.; Kerkamm, I.; Xu, Y.; van der Maas, E.; Kelder, E. M.; Ganapathy, S.; Wagemaker, M.; Wagemaker, M. Clarifying the relationship between redox activity and electrochemical stability in solid electrolytes. *Nat. Mater.* **2020**, *19*, 428−435.

(67) Zhu, Y.; He, X.; Mo, Y. Origin of outstanding stability in the lithium solid electrolyte materials: insights from thermodynamic analyses based on first-principles calculations. *ACS Appl. Mater. Interfaces* **2015**, *7*, 23685−23693.

(68) Xiao, Y.; Wang, Y.; Bo, S.-H.; Kim, J. C.; Miara, L. J.; Ceder, G. Understanding interface stability in solid-state batteries. *Nat. Rev. Mater.* **2020**, *5*, 105−126.

(69) Mangani, L. R.; Villevieille, C. Mechanical vs. chemical stability of sulphide-based solid-state batteries. Which one is the biggest challenge to tackle? Overview of solid-state batteries and hybrid solid state batteries. *J. Mater. Chem. A* **2020**, *8*, 10150−10167.

(70) Opalka, D.; Scheurer, C.; Reuter, K. Ab initio thermodynamics insight into the structural evolution of working IrO2 catalysts in proton-exchange membrane electrolyzers. *ACS Catal.* **2019**, *9*, 4944−4950.